

Bright multiplexed source of indistinguishable single photons with tunable GHz-bandwidth at room temperature

O. Davidson,¹ R. Finkelstein,¹ E. Poem,¹ and O. Firstenberg¹

¹*Physics of Complex Systems, Weizmann Institute of Science, Rehovot 7610001, Israel*

Narrowband single photons that couple well to atomic ensembles could prove essential for future quantum networks, but the efficient generation of such photons remains an outstanding challenge. We realize a spatially-multiplexed heralded source of single photons that are inherently compatible with the commonly employed D2 line of rubidium. Our source is based on four-wave mixing in hot rubidium vapor, requiring no laser cooling or optical cavities, and generates single photons with high rate and low noise. We use Hong-Ou-Mandel interference to verify the indistinguishability of the photons generated in two different (multiplexed) channels. We further demonstrate a five-fold tunability of the photons' temporal width. The experimental results are well reproduced by a theoretical model.

I. INTRODUCTION

Single photons are key ingredients in quantum optics experiments and in quantum communication protocols, such as quantum repeaters and quantum key distribution (QKD) [1]. A prevalent method for generating single photons is spontaneous parametric down-conversion (SPDC) in $\chi^{(2)}$ nonlinear crystals [2]. However, the photons generated in SPDC are inherently broadband, and thus it is difficult to interface them with atomic ensembles, as required for many quantum communication and computation protocols. Narrowing the source bandwidth by placing the nonlinear crystals inside an optical cavity generally comes at the cost of a reduction in other performance parameters and in technical overhead [3–12].

Another successful route for single-photon generation is utilizing single quantum emitters. A prime example is semiconductor quantum-dots in micro-cavities [13–15] able to generate photons with a bandwidth of several GHz, which could, in principle, couple to atomic ensembles. However, only limited success has been achieved to date in interfacing these photons with atomic ensembles [16, 17]. Moreover, it is difficult to achieve indistinguishable photons from two distinct quantum dots, making these source's scaling-up challenging. Another type of single emitters is single trapped atoms [18, 19] and ions [20, 21], which generate single photons that are inherently compatible with atomic systems. However, these systems require a relatively complex apparatus and their photon collection efficiency and generation rate are relatively low.

As an alternative to single emitters, correlated photon pairs can be generated using atomic ensembles [22–41]. In the Duan-Lukin-Cirac-Zoller protocol [42], the photons generation is done with a write-read pulse sequence: the first photon heralds the existence of a spin-wave in the atomic ensemble, which is later converted into a second photon. Alternatively, photon pairs can be generated in continuous operation by a four-wave mixing (FWM) process, where detecting one photon heralds the existence of the other. Such heralded sources were realized with cold [22–26, 30, 31] and hot atomic ensembles [34–36]. Hot atomic vapor provides a simpler setup and can operate continuously, although often motional-broadening reduces the atomic coherence and consequently lowers the signal-to-noise ratio (SNR).

Here we study a heralded single-photon source based on

FWM in hot ^{85}Rb vapor. We employ the nearly Doppler-free configuration of the $5S_{1/2} - 5P_{3/2} - 5D_{5/2}$ ladder scheme. This system was first used as a photon source by Lee *et al.* [36–39]. As shown in Fig. 1, we simultaneously achieve high generation rate and high SNR (quantified by the bi-photon cross-correlation). Furthermore, we demonstrate the multiplexing capability of the source by collecting single photons from two spatial channels and verifying their indistinguishability using Hong-Ou-Mandel (HOM) interference. We investigate the system performance for different optical depths of the atomic ensemble and demonstrate the ability to control the photons' temporal width. The experimental study is accompanied by a detailed model reproducing the measurements. This system is adequate for interfacing with other quantum systems and particularly with Rb atoms. When com-

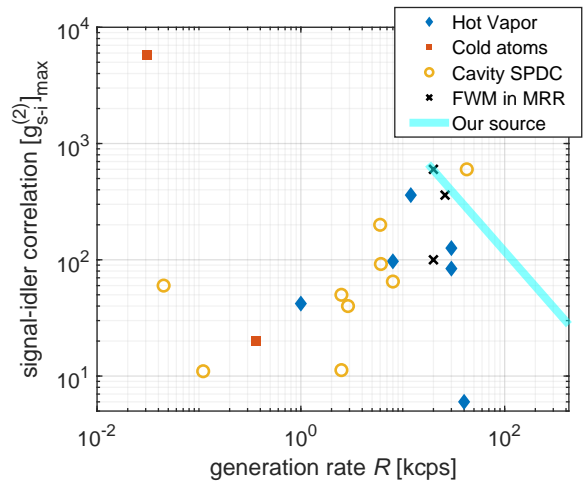


Figure 1. **Comparison of heralded single-photon sources** in terms of the peak of the normalized bi-photon cross-correlation function $[g_{s-i}^{(2)}]_{\max}$ and the generation rate of heralded single photons R . Getting to the top right corner is desirable. We include bi-photon sources with a bandwidth on the order of a few GHz or smaller, capable in principle of interfacing efficiently with atomic ensembles. R is the actual detection rate in kilo-counts per second (kcps). Sources: Hot vapor [33, 35, 36, 39–41], cold atoms [28, 29], cavity SPDC [4–12], FWM in MRR (Microring resonators) [43–45]. See Supplementary Material for more details.

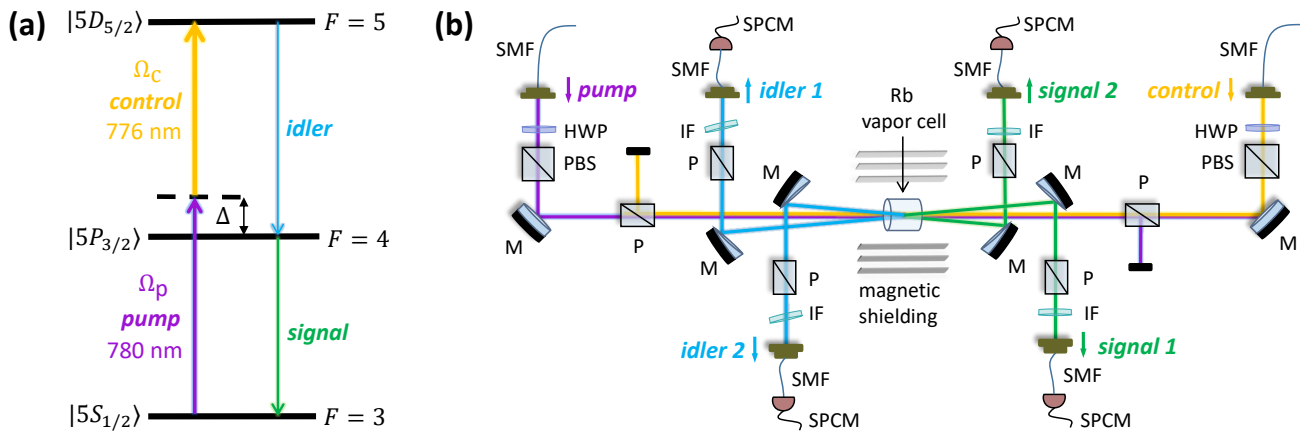


Figure 2. **Energy levels and experimental setup.** (a) The relevant atomic levels of ^{85}Rb . In the presence of pump and control lasers, phase-matched signal and idler photons are spontaneously generated. (b) The experimental setup. The pump and control lasers counter-propagate inside the vapor cell. Signal and idler photons are generated in the cone-shaped phase-matched direction and collected from two spatial modes into single-mode fibers. HWP: half-wave plate, IF: interference filter (FWHM 3 nm), M: mirror, P: Glan calcite polarizer, PBS: polarizing beam splitter, SMF: single-mode fiber, SPCM: single-photon counting module.

bined with a quantum memory [46], it can be used to construct large multi-photon states applicable for secure QKD.

II. SETUP

We use the rubidium level system shown in Fig. 2(a). The pump field, coupling the $5S_{1/2} \rightarrow 5P_{3/2}$ transition, originates from a 780-nm distributed Bragg reflector laser. It is blue detuned by $\Delta = 1$ GHz from the transition in order to minimize the absorption to the $5P_{3/2}$ level while maintaining a large third-order susceptibility $\chi^{(3)}$. The control field, coupling the $5P_{3/2} \rightarrow 5D_{5/2}$ transition, originates from an external-cavity diode-laser at 776 nm. It is tuned such that the two-photon transition is on resonance for maximizing $\chi^{(3)}$. The two lasers are independently phase-locked to stable reference lasers, which are locked to ultra-stable cavities. We do not perform dedicated optical pumping, and therefore all the Zeeman states in the ground level are roughly equally populated.

Figure 2(b) shows the experimental setup. The vertically-polarized pump and horizontally-polarized control fields, with beam waist radii of 0.45 mm, counter-propagate through a 25-mm-long cell of pure ^{85}Rb vapor. The cell is placed inside a three-layer mu-metal magnetic shield mounted on a pitch-yaw rotation stage, which is used to minimize the scattering of light off the vapor-cell facets into the signal and idler modes. We vary the optical depth of the medium in the range $\text{OD} = 1 - 15$ (measured for the $|5S_{1/2}, F = 3\rangle \rightarrow |5P_{3/2}, F = 2, 3, 4\rangle$ transitions) by tuning the cell temperature. The signal and idler photons are spontaneously generated in a FWM process in the phase-matched directions. After polarization and wavelength filtering [interference filters, full width at half maximum (FWHM) of 3 nm], the horizontally-polarized signal and vertically-polarized idler photons are coupled into single-mode fibers (SMF) that act as spatial filters.

Due to the wavelength mismatch in the ladder scheme and

due to carefully tuning the vapor cell orientation, we do not need to use narrow-band Fabry-Perot cavities to filter out the pump and control light. This increases the setup transmission and contributes to the high generation rate we achieve. The signal and idler photons are collected at $\sim 1.4^\circ$ off-axis from both sides, thus forming two spatially multiplexed collection channels. This angle is chosen as a compromise between maximizing the phase-matching condition, which is practically on axis, and minimizing the noise due to the pump and control light. The signal and idler photons are then detected by single-photon counting modules (SPCM; Excelitas NIR-14-FC) with a $\sim 68\%$ quantum efficiency. The SPCMs are connected to a time tagging device (Swabian Time Tagger Ultra). The combined detection jitter of the time tagger and the two SPCMs was measured with a sub-ps laser to be approximately a sech function with FWHM of 590 ps.

To align the signal and idler output-couplers, we pick off some of the control (pump) light and use it to seed the idler (signal) mode in the first (second) collection channel. A stimulated FWM signal is then generated in the phase-matched direction and coupled into the corresponding SMF. Subsequently, since the spontaneously generated photons have slightly different modes than the (collimated) seed beams, we perform the final optimization of the phase-matching conditions by maximizing the spontaneous bi-photon generation rate R without the seed light. This procedure increases R by more than 40%.

III. RESULTS

We begin with measurements of the cross-correlation and generation rate of the bi-photons. The normalized signal-idler cross-correlation function is defined as $g_{s-i}^{(2)}(\tau) = \langle a_i^\dagger(t)a_s^\dagger(t+\tau)a_s(t+\tau)a_i(t) \rangle / [\langle a_s^\dagger a_s \rangle \langle a_i^\dagger a_i \rangle]$, where $\tau = t_s - t_i$ is the time difference between the detection of the signal and idler pho-

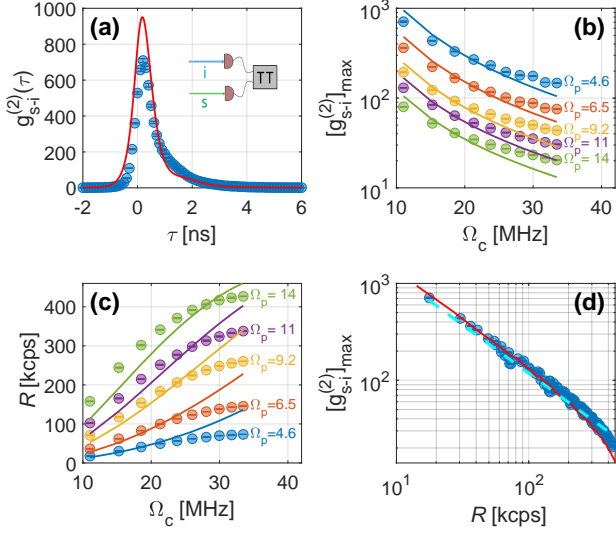


Figure 3. Bi-photon cross-correlation. (a) The normalized cross-correlation between the signal and idler photons $g_{s-i}^{(2)}(\tau)$ versus $\tau = t_s - t_i$, where t_s (t_i) is the signal (idler) photon detection time. Here the Rabi frequencies of the pump and control fields are $\Omega_p = 4.6$ MHz (power 0.05 mW) and $\Omega_c = 11.5$ MHz (power 5 mW), respectively. The inset shows a schematic of the detection scheme, where TT stands for time tagger. (b) The peak of the normalized cross-correlation function $[g_{s-i}^{(2)}]_{\max}$ versus Ω_p and Ω_c (values given in MHz). (c) The bi-photon generation rate R as a function of Ω_p and Ω_c . (d) $[g_{s-i}^{(2)}]_{\max}$ versus R in the full parameter range ($\Omega_p = 5 - 15$ MHz and $\Omega_c = 10 - 35$ MHz). In all plots, circles are measured data, and solid curves are numerical calculations (see text for details of the calculations). Dashed line in (d) is a fit to a pure R^{-1} curve. Here OD = 9.3. Error bars correspond to 1 standard deviation (s.d.).

tons, and $\langle \cdot \rangle$ indicates averaging over the time t . Figure 3(a) shows $g_{s-i}^{(2)}(\tau)$ measured at OD = 9.3 (cell temperature $\sim 55^\circ\text{C}$) and low pump and control powers. A strong signal-idler temporal correlation is evident, with a peak value $[g_{s-i}^{(2)}]_{\max} = 709 \pm 10$, higher than previously-reported values in atomic vapor systems. The peak value $[g_{s-i}^{(2)}]_{\max}$ is often associated with the SNR of the source [34], and our source violates the classical Cauchy-Schwartz inequality $[[g_{s-i}^{(2)}]_{\max}]^2 / [g_{s-s}^{(2)}(0)g_{i-i}^{(2)}(0)] \leq 1$ [47] by a factor greater than 10^5 . When increasing the pump and control powers, $[g_{s-i}^{(2)}]_{\max}$ decreases, as shown in Fig. 3(b), while the bi-photon generation rate R increases, as shown in Fig. 3(c). For R , we consider only detected pairs and subtract the background coincidence counts. The trade-off between R and $[g_{s-i}^{(2)}]_{\max}$, *i.e.*, between the rate and the SNR, is summarized in Fig. 3(d); the dashed line in this figure is a fit to a pure inverse relation ($\propto R^{-1}$).

In order to demonstrate that the bi-photon source can be used as a heralded single photon source, we measure the auto-correlation of signal photons, conditioned on the detection of an idler photon. In this measurement, we use a Hanbury Brown and Twiss setup, where the signal photons are sent into a fiber beam-splitter connected to two SPCMs.

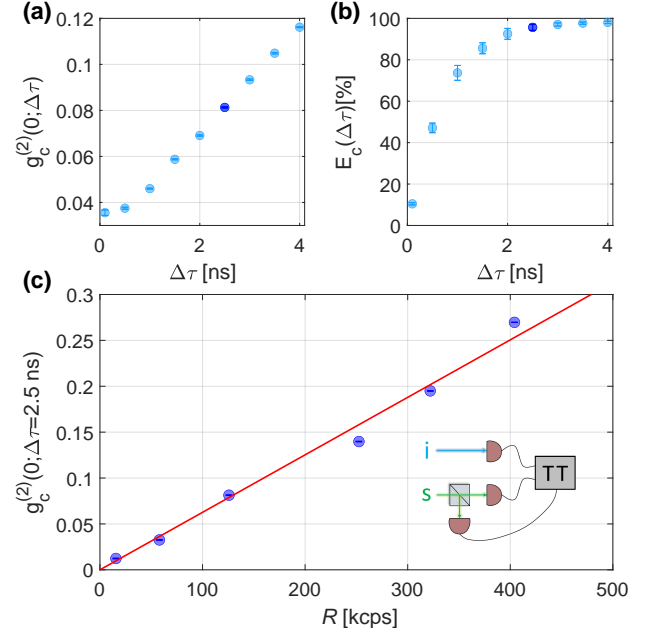


Figure 4. The single-photon nature of the heralded source. (a) The auto-correlation of signal photons $g_c^{(2)}(0; \Delta\tau)$, conditioned on the detection of an idler photon within a temporal coincidence window $\Delta\tau$. Here the pump and control Rabi frequencies are $\Omega_p = 6.5$ MHz and $\Omega_c = 30$ MHz, respectively. (b) The overall signal counts E_c within $\Delta\tau$ normalized by the counts in a wide coincidence window ($\Delta\tau > 4$ ns). Less than 5% of the heralded single photons are trimmed for a choice of $\Delta\tau \geq 2.5$ ns. (c) The conditional auto-correlation function versus the heralded single-photon generation rate R for $\Delta\tau = 2.5$ ns. Dark-blue data points in (a) and (b) correspond to $\Delta\tau = 2.5$ ns used in (c). Error bars are 1 s.d. The solid line is a linear fit to the data. The inset in (c) shows a schematic of the detection scheme.

For a given temporal coincidence-window $\Delta\tau$, the conditional auto-correlation is given by $g_c^{(2)}(0; \Delta\tau) = N_{i-s_1-s_2}N_i / [N_{i-s_1}N_{i-s_2}]$ [48]. Here N_i is the idler count rate, $N_{i-s_1}(\Delta\tau)$ and $N_{i-s_2}(\Delta\tau)$ are the count rates of coincidences of an idler photon and a signal photon in one of the two SPCMs in a coincidence time window $\Delta\tau$, and $N_{i-s_1-s_2}(\Delta\tau)$ is the three-photon coincidence count rate. Figure 4(a) shows that $g_c^{(2)}(0; \Delta\tau) \ll 1$ for all coincidence windows in the range $0 < \Delta\tau \leq 4$ ns, indicating strong anti-bunching. As $\Delta\tau$ decreases, we measure a smaller fraction $E_c(\Delta\tau)$ of the single-photon wave-packet [$E_c(\infty) = 100\%$]; this fraction is given in Fig. 4(b). For $\Delta\tau = 2.5$ ns, $95.6 \pm 1.4\%$ of the heralded single photon intensity is measured. Figure 4(c) shows $g_c^{(2)}(0; \Delta\tau)$ as a function of the bi-photon generation rate R for $\Delta\tau = 2.5$ ns. The minimal value measured is $g_c^{(2)}(0; \Delta\tau) = 0.012 \pm 0.0003$, with $R = 15$ kcps. Even with $R = 400$ kcps, $g_c^{(2)}(0; \Delta\tau) = 0.27$ is still well below the two-photon threshold of $g_c^{(2)}(0; \Delta\tau) = 0.5$, thus validating the single-photon nature of the source.

The detection of an idler photon heralds the generation of a collective state comprising a single $5P_{3/2}$ excitation that is shared among all atoms. The subsequent spontaneous emis-

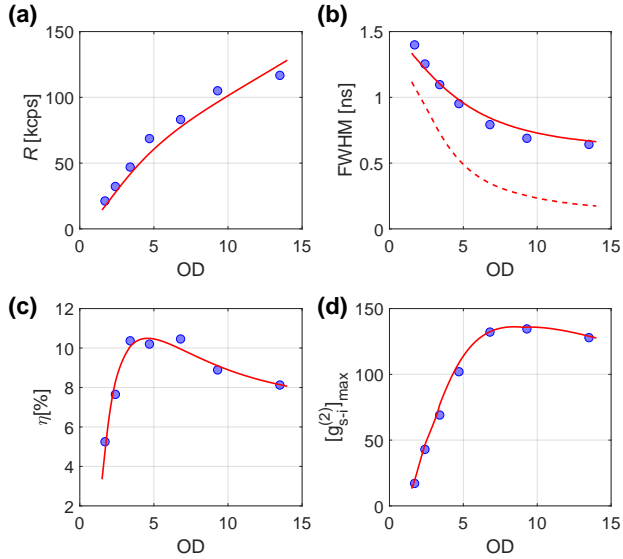


Figure 5. **Source performance as a function of optical depth.** (a) Heralded single-photon generation rate R . (b) Duration of the heralded single-photons. The dashed line shows the inferred duration after removing the electronic detection time-jitter, demonstrating tunability of the photon duration by more than $\times 5$. (c) Signal photon heralding efficiency η , reaching an optimum at $OD \approx 5$. (d) The peak of the normalized cross-correlation function for a constant R , reaching an optimum at $OD \approx 7 - 11$. Circles are measured values, and curves are numerical calculations. In (a) and (b), the pump and control Rabi frequencies are $\Omega_p = 6.5$ MHz and $\Omega_c = 21$ MHz, respectively. In (c) and (d), Ω_p and Ω_c are adjusted to keep a constant $R = 100$ kcps.

sion of a signal photon from this state into the phased-matched direction is collectively enhanced [49]. The number of atoms, quantified by the OD, thus plays an important role in the source performance, which we now examine. As expected and as shown in Figs. 5(a,b), the heralded photon generation rate increases with OD, while the duration (temporal width) of the heralded photons decreases. Taking into account the combined electronic time-jitter for two detectors (590 ps), we find that the photon's duration can be varied five-fold by changing the OD [dashed line in Fig. 5(b)].

We now turn to measure the heralding efficiency, defined as $\eta = R/N_i$, which quantifies the probability to get a signal photon given a detection of an idler photon. To be conservative, we consider only detected events and do not correct for the setup transmission or detectors inefficiencies. For a fixed generation rate $R = 100$ kcps, the heralding efficiency as a function of OD shows an optimum $\eta \approx 10.5\%$ at $OD \approx 5$, see Fig. 5(c). The decrease in η at high OD can be explained by reabsorption of the signal photon in the medium, whereas the increase at low OD is explained by the enhancement in the collective emission into the phase-matched direction [49]. Figure 5(d) shows $[g_{s-i}^{(2)}]_{\max}$ versus OD. Here also, there is an optimal OD that maximizes the SNR, at $OD \approx 7 - 11$. This optimal OD is higher than that found for the heralding efficiency due to the enhanced emission rate of the photons at

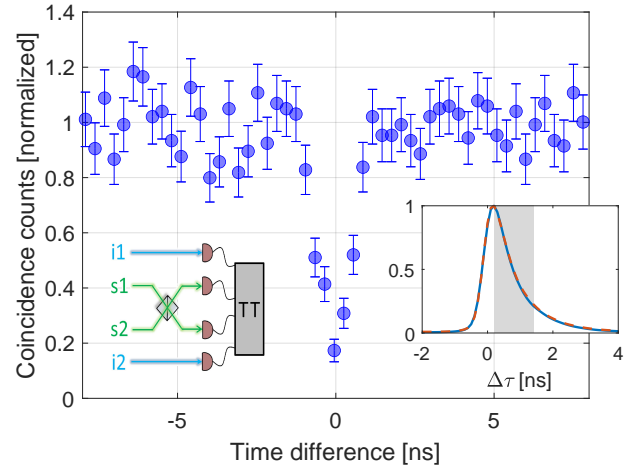


Figure 6. **Photons indistinguishability.** Coincidence counts of the heralded photons (in the two signal channels) as a function of the time difference between the heralding photons (idler photons) in a HOM interference setup. Interference visibility of $V = 82.7 \pm 4.1\%$ is observed without any background subtraction, demonstrating high indistinguishability between the two channels. Error bars are 1 s.d., estimated from Poissonian counting statistics. The inset shows the shape of the heralded photons in the two signal channels, exhibiting a temporal likeness of $> 99\%$. The temporal window considered for a coincidences detection (gray shaded area) starts at the peak of the cross-correlation function because of the asymmetry resulting from the cascaded emission of the idler and signal photons and considering that the detection time jitter (590 ps) is large compared to the photons' duration.

higher OD.

Next, we turn to demonstrate the multiplexing capability of the source by using two collection channels of idler-photon pairs and using HOM interference to characterize the indistinguishability of the generated photons. Figure 6 shows the four-fold coincidence counts of the heralded single photons in a HOM setup, where the two signal photons generated in the two collection channels enter a 50:50 fiber-BS from different input ports [50]. The two BS outputs are connected to SPCMs. The horizontal axis is the time difference between the detection of the two idler photons, which heralds the generation of the two signal photons. The raw HOM visibility is $V = 82.7 \pm 4.1\%$. The main factor that reduces V from unity is the large detection time-jitter compared to the photons duration, which reduces the heralded photons' purity by $\sim 20\%$ [51], thus limiting the HOM visibility to $V \sim 80\%$ [52]. For this reason, the measurement was done with $OD = 4.7$, for which the photons are relatively long, while the SNR is still high. The inset of Fig. 6 shows the shape of the heralded photons generated in the two collection channels. The temporal likeness of the two photons, defined as $|\int \sqrt{G_1(t)}\sqrt{G_2(t)}dt|^2 / [\int G_1(t)dt \int G_2(t)dt]$, where $G_{1(2)}$ is the non-normalized cross-correlation function in channel 1(2), is $> 99\%$. Here $\Omega_p = 7$ MHz and $\Omega_c = 10.5$ MHz, and the generation rates in the two channels are $R = 27$ kcps and $R = 20$ kcps.

IV. MODEL

We base our model on the state-vector formalism of the FWM interaction [53]. We provide here a brief description of the model, while details are given in as Supplementary Material (SM).

Let ω_s , ω_i , ω_p , and ω_c be the frequencies of the signal, idler, pump, and control fields, respectively. We write the wave numbers of these fields as $k_s = \sqrt{1 + \chi_s(\omega_s)}\omega_s/c$, $k_i = \sqrt{1 + \chi_i(\omega_i)}\omega_i/c$, $k_p = \omega_p/c$, and $k_c = \omega_c/c$, where for the signal and idler fields we include the linear susceptibility of the atomic medium, incorporating the effects of gain, loss, and dispersion. The bi-photon wavefunction is given by [53]

$$\psi(\tau) = \frac{L}{2\pi} \int d\omega_s \kappa(\omega_s) \text{sinc}\left(\frac{\Delta k L}{2}\right) e^{i(k_s + k_i)L/2} e^{-i\omega_s \tau}, \quad (1)$$

where L is the length of the atomic medium, and $\Delta k = (k_s - k_i) - (k_p - k_c)$ is the phase mismatch of the FWM process, assuming that the angular deviation of the fields from the \hat{z} axis is small. The term $e^{i(k_s + k_i)L/2}$ represents the free propagation of the signal and idler fields, the phase matching condition is manifested in $\text{sinc}(\Delta k L/2)$, and $\kappa(\omega_s) \propto \chi^{(3)}(\omega_s)$ represents the nonlinear interaction; the full expression of $\kappa(\omega_s)$ is given in the SM.

Previously published calculations of $\chi^{(3)}$ have assumed that the atomic population remains in the ground state, *i.e.*, that the pump field is weak [32, 53]. Here, we do not make this assumption. We use the finite population in the excited states to model the signal and idler detection count rates and, together with the bi-photon wavefunction [Eq. (1)], we numerically calculate the scaling of $[g_{s-i}^{(2)}]_{\max}$ and the heralding efficiency with the pump and control powers and with the OD. Detailed expressions of $\chi^{(3)}$ and exact expressions for the numerical curves in Figs. 3 and 5 are given in the SM. No fit parameters are used in these calculations except for fixed rescaling factors of $g_{s-i}^{(2)}$, R , and η . The scaling factors are the same for all presented data and account for photon collection efficiency and for the conversion ratio of the excited-state population to the signal and idler detection rates.

V. DISCUSSION

We now return to Fig. 1, comparing between different heralded single-photon sources in terms of the generation rate R (actual detection rates, without any corrections) and $[g_{s-i}^{(2)}]_{\max}$, which quantifies the SNR. Here we limit ourselves to sources with bandwidth on the order of a few GHz or lower, which, in principle, could be interfaced with atomic ensembles or with high-efficiency solid-state memories. Our source outperforms all other atomic sources in this metric and is comparable to the best solid-state sources.

Several factors enable the high generation rate and SNR of our source. First, the nearly Doppler-free level scheme of the $5S_{1/2} - 5P_{3/2} - 5D_{5/2}$ excitation maintains the spin-wave coherence for a long time. Second, we minimize photon loss by

not using narrow-band etalons, which are usually employed to filter out the noise originating from the scattering of the driving fields. Third, we optimize the powers and detunings of the driving fields and the OD of the medium. Finally, our pump and control lasers are independently locked to ultra-stable references, further increasing the spin-wave coherence of the $5S \rightarrow 5D$ transition.

Residual scattering of the driving fields from the vapor cell's facets weakly couples into the collection channels, generating noise that degrades the source performance. The noise becomes a limitation at a pump power below $50 \mu\text{W}$ and at a control power above 40 mW . This noise can be minimized by small changes in the collection angles at the expense of deteriorating the phase-matching conditions (in our optimizations, minimizing the noise reduces R by $\sim 25 - 30\%$). These limitations can be overcome by using better wall coatings to reduce the scattering of the driving fields. Moreover, the HOM interference visibility can be greatly improved by using detectors with a lower electronic detection time jitter, such as superconducting nanowire detectors.

Our source, like the majority of photon sources, has a greater than 50% vacuum component. This property makes the generated heralded photons less suitable for quantum computation applications [54]. In the future, this limitation may be elevated by using detectors with higher quantum efficiency and by enclosing the signal and idler modes in cavities. At the source's current level of the performance, up to $R \approx 200 \text{ kcps}$, our heralded single photons are in a quantum non-Gaussian (QNG) state, as estimated from our $g_c^{(2)}(0; \Delta\tau)$ measurements using the QNG state criterion $P_c < P_s^3/3$ (for $P_c \ll P_s$) [21, 55]. Here, $P_s \approx 0.09$ is the probability, upon a heralding event, to detect exactly one photon in the signal mode, and $P_c \approx 2.5 \times 10^{-5} - 1.6 \times 10^{-4}$ (for $R = 15 - 126 \text{ kcps}$) is the probability to detect two photons. The QNG criterion, which is stricter than the non-classical condition of $g_c^{(2)}(0) < 1$ [55], is a sufficient condition for the security of QKD [56], thus making our source a potential resource for QKD applications.

In conclusion, we demonstrate a highly bright, spatially-multiplexed, heralded single-photon source, emitting indistinguishable photons with a tunable bandwidth. The generated photons are inherently compatible for interfacing with rubidium atomic ensembles, and we simultaneously achieve high SNR and high generation rate. These properties make the source adequate for atom-photon quantum networks. Furthermore, the generated photons are in a QNG state, making them suitable for secure QKD.

ACKNOWLEDGMENTS

We thank Lee Drori and Ohr Lahad for useful discussions and technical assistance. We acknowledge financial support by the the Israel Science Foundation, the US-Israel Binational Science Foundation (BSF) and US National Science Foundation (NSF), the European Research Council starting investigator grant QPHOTONICS 678674, the Minerva Foundation with funding from the Federal German Ministry for Education and Research, and the Laboratory in Memory of Leon and Blacky Broder.

- [1] M. D. Eisaman, J. Fan, A. Migdall, and S. V. Polyakov. Invited review article: Single-photon sources and detectors. *Review of Scientific Instruments*, 82(7):071101, 2011.
- [2] Oliver Slattery, Lijun Ma, Kevin Zong, and Xiao Tang. Background and review of cavity-enhanced spontaneous parametric down-conversion. *J. Res. Natl. Inst. Stan.*, 124:124019, 2019.
- [3] Z. Y. Ou and Y. J. Lu. Cavity enhanced spontaneous parametric down-conversion for the prolongation of correlation time between conjugate photons. *Phys. Rev. Lett.*, 83:2556–2559, 1999.
- [4] J. S. Neergaard-Nielsen, B. Melholt Nielsen, H. Takahashi, A. I. Vistnes, and E. S. Polzik. High purity bright single photon source. *Opt. Express*, 15(13):7940–7949, 2007.
- [5] Daniel Rieländer, Andreas Lenhard, Margherita Mazzera, and Hugues de Riedmatten. Cavity enhanced telecom heralded single photons for spin-wave solid state quantum memories. *New Journal of Physics*, 18(12):123013, 2016.
- [6] Chih-Hsiang Wu, Tsung-Yao Wu, Yung-Chin Yeh, Po-Hui Liu, Chin-Hsuan Chang, Chiao-Kai Liu, Ting Cheng, and Chih-Sung Chuu. Bright single photons for light-matter interaction. *Phys. Rev. A*, 96:023811, 2017.
- [7] Pin-Ju Tsai and Ying-Cheng Chen. Ultrabright, narrow-band photon-pair source for atomic quantum memories. *Quantum Science and Technology*, 3(3):034005, 2018.
- [8] Roberto Mottola, Gianni Buser, Chris Müller, Tim Kroh, Andreas Ahlrichs, Sven Ramelow, Oliver Benson, Philipp Treutlein, and Janik Wolters. An efficient, tunable, and robust source of narrow-band photon pairs at the 87rb d1 line. *Opt. Express*, 28(3):3159–3170, 2020.
- [9] Jianji Liu, Jiachen Liu, Ping Yu, and Guoquan Zhang. Sub-megahertz narrow-band photon pairs at 606 nm for solid-state quantum memories. *APL Photonics*, 5(6):066105, 2020.
- [10] Amir Moqanaki, Francesco Massa, and Philip Walther. Novel single-mode narrow-band photon source of high brightness tuned to cesium d2 line. *APL Photonics*, 4(9):090804, 2019.
- [11] Xiao Liu, Jun Hu, Zong-Feng Li, Xue Li, Pei-Yun Li, Peng-Jun Liang, Zong-Quan Zhou, Chuan-Feng Li, and Guang-Can Guo. Experimental demonstration of functional quantum repeater nodes with absorptive quantum memories. *arXiv:2101.04945*, 2021.
- [12] Yin-Hai Li, Zhi-Yuan Zhou, Shi-Long Liu, Yan Li, Shi-Kai Liu, Chen Yang, Shuang Wang, Zhi han Zhu, Wei Gao, Guang-Can Guo, and Bao-Sen Shi. Compact sub-ghz bandwidth single-mode time-energy entangled photon source for high-speed quantum networks. *OSA Continuum*, 4(2):608–620, 2021.
- [13] N. Somaschi, V. Giesz, L. De Santis, J. C. Loredó, M. P. Almeida, G. Hornecker, S. L. Portalupi, T. Grange, C. Antón, J. Demory, C. Gómez, I. Sagnes, N. D. Lanzillotti-Kimura, A. Lemaître, A. Auffeves, A. G. White, L. Lanco, and P. Senellart. Near-optimal single-photon sources in the solid state. *Nature Photonics*, 10(5):340–345, 2016.
- [14] Xing Ding, Yu He, Z.-C. Duan, Niels Gregersen, M.-C. Chen, S. Unsleber, S. Maier, Christian Schneider, Martin Kamp, Sven Höfling, Chao-Yang Lu, and Jian-Wei Pan. On-demand single photons with high extraction efficiency and near-unity indistinguishability from a resonantly driven quantum dot in a micropillar. *Phys. Rev. Lett.*, 116:020401, 2016.
- [15] Natasha Tomm, Alisa Javadi, Nadia Olympia Antoniadis, Daniel Najer, Matthias Christian Löbl, Alexander Rolf Korsch, Rüdiger Schott, Sascha René Valentín, Andreas Dirk Wieck, Arne Ludwig, and Richard John Warburton. A bright and fast source of coherent single photons. *Nature Nanotechnology*, 2021.
- [16] N. Akopian, L. Wang, A. Rastelli, O. G. Schmidt, and V. Zwiller. Hybrid semiconductor-atomic interface: slowing down single photons from a quantum dot. *Nature Photonics*, 5(4):230–233, 2011.
- [17] Hüseyin Vural, Simone L. Portalupi, Julian Maisch, Simon Kern, Jonas H. Weber, Michael Jetter, Jörg Wrachtrup, Robert Löw, Ilja Gerhardt, and Peter Michler. Two-photon interference in an atom-quantum dot hybrid system. *Optica*, 5(4):367–373, 2018.
- [18] J. McKeever, A. Boca, A. D. Boozer, R. Miller, J. R. Buck, A. Kuzmich, and H. J. Kimble. Deterministic generation of single photons from one atom trapped in a cavity. *Science*, 303(5666):1992–1994, 2004.
- [19] Markus Hiljkema, Bernhard Weber, Holger P. Specht, Simon C. Webster, Axel Kuhn, and Gerhard Rempe. A single-photon server with just one atom. *Nature Physics*, 3(4):253–255, 2007.
- [20] P. Maunz, D. L. Moehring, S. Olmschenk, K. C. Younge, D. N. Matsukevich, and C. Monroe. Quantum interference of photon pairs from two remote trapped atomic ions. *Nature Physics*, 3(8):538–541, 2007.
- [21] D B Higginbottom, L Slodička, G Araneda, L Lachman, R Filip, M Hennrich, and R Blatt. Pure single photons from a trapped atom source. *New Journal of Physics*, 18(9):093038, 2016.
- [22] C. W. Chou, S. V. Polyakov, A. Kuzmich, and H. J. Kimble. Single-photon generation from stored excitation in an atomic ensemble. *Phys. Rev. Lett.*, 92:213601, 2004.
- [23] T. Chanelière, D. N. Matsukevich, S. D. Jenkins, S.-Y. Lan, T. A. B. Kennedy, and A. Kuzmich. Storage and retrieval of single photons transmitted between remote quantum memories. *Nature*, 438(7069):833–836, 2005.
- [24] James K. Thompson, Jonathan Simon, Huanqian Loh, and Vladan Vuletić. A high-brightness source of narrowband, identical-photon pairs. *Science*, 313(5783):74–77, 2006.
- [25] Erwan Bimbard, Rajiv Boddeda, Nicolas Vitrant, Andrey Grankin, Valentina Parigi, Jovica Stanojevic, Alexei Ourjoumtsev, and Philippe Grangier. Homodyne tomography of a single photon retrieved on demand from a cavity-enhanced cold atom memory. *Phys. Rev. Lett.*, 112:033601, 2014.
- [26] Pau Farrera, Georg Heinze, Boris Albrecht, Melvyn Ho, Matías Chávez, Colin Teo, Nicolas Sangouard, and Hugues de Riedmatten. Generation of single photons with highly tunable wave shape from a cold atomic ensemble. *Nature Communications*, 7(1):13556, 2016.
- [27] Jian-Peng Dou, Ai-Lin Yang, Mu-Yan Du, Di Lao, Jun Gao, Lu-Feng Qiao, Hang Li, Xiao-Ling Pang, Zhen Feng, Hao Tang, and Xian-Min Jin. A broadband dlcz quantum memory in room-temperature atoms. *Communications Physics*, 1(1):55, 2018.
- [28] Vlatko Balić, Danielle A. Braje, Pavel Kolchin, G. Y. Yin, and S. E. Harris. Generation of paired photons with controllable waveforms. *Phys. Rev. Lett.*, 94:183601, 2005.
- [29] Bharath Srivathsan, Gurpreet Kaur Gulati, Brenda Chng, Gleb Maslennikov, Dzmityr Matsukevich, and Christian Kurtsiefer. Narrow band source of transform-limited photon pairs via four-wave mixing in a cold atomic ensemble. *Phys. Rev. Lett.*, 111:123602, 2013.
- [30] Gurpreet Kaur Gulati, Bharath Srivathsan, Brenda Chng,

- Alessandro Cerè, Dzmitry Matsukevich, and Christian Kurtz. Generation of an exponentially rising single-photon field from parametric conversion in atoms. *Phys. Rev. A*, 90:033819, 2014.
- [31] Peng Qian, Zhenjie Gu, Rong Cao, Rong Wen, Z. Y. Ou, J. F. Chen, and Weiping Zhang. Temporal purity and quantum interference of single photons from two independent cold atomic ensembles. *Phys. Rev. Lett.*, 117:013602, 2016.
- [32] Dong-Sheng Ding, Zhi-Yuan Zhou, Bao-Sen Shi, Xu-Bo Zou, and Guang-Can Guo. Generation of non-classical correlated photon pairs via a ladder-type atomic configuration: theory and experiment. *Opt. Express*, 20(10):11433–11444, 2012.
- [33] Dong-Sheng Ding, Wei Zhang, Shuai Shi, Zhi-Yuan Zhou, Yan Li, Bao-Sen Shi, and Guang-Can Guo. Hybrid-cascaded generation of tripartite telecom photons using an atomic ensemble and a nonlinear waveguide. *Optica*, 2(7):642–645, 2015.
- [34] Chi Shu, Peng Chen, Tsz Kiu Aaron Chow, Lingbang Zhu, Yanhong Xiao, M. M. T. Loy, and Shengwang Du. Subnaturallinewidth biphotons from a doppler-broadened hot atomic vapour cell. *Nature Communications*, 7(1):12783, 2016.
- [35] Lingbang Zhu, Xianxin Guo, Chi Shu, Heejeong Jeong, and Shengwang Du. Bright narrowband biphoton generation from a hot rubidium atomic vapor cell. *Appl. Phys. Lett.*, 110(16):161101, 2017.
- [36] Yoon-Seok Lee, Sang Min Lee, Heonoh Kim, and Han Seb Moon. Highly bright photon-pair generation in doppler-broadened ladder-type atomic system. *Opt. Express*, 24(24):28083–28091, 2016.
- [37] Taek Jeong, Yoon-Seok Lee, Jiho Park, Heonoh Kim, and Han Seb Moon. Quantum interference between autonomous single-photon sources from doppler-broadened atomic ensembles. *Optica*, 4(10):1167–1170, 2017.
- [38] Jiho Park, Taek Jeong, Heonoh Kim, and Han Seb Moon. Time-energy entangled photon pairs from doppler-broadened atomic ensemble via collective two-photon coherence. *Phys. Rev. Lett.*, 121:263601, 2018.
- [39] Jiho Park, Heonoh Kim, and Han Seb Moon. Polarization-entangled photons from a warm atomic ensemble using a sagnac interferometer. *Phys. Rev. Lett.*, 122:143601, 2019.
- [40] J Mika and L Slodička. High nonclassical correlations of large-bandwidth photon pairs generated in warm atomic vapor. *Jr. Phys. B: At. Mol. Opt. Phys.*, 53(14):145501, 2020.
- [41] Chia-Yu Hsu, Yu-Sheng Wang, Jia-Mou Chen, Fu-Chen Huang, Yi-Ting Ke, Emily Kay Huang, Weilun Hung, Kai-Lin Chao, Shih-Si Hsiao, Yi-Hsin Chen, Chih-Sung Chuu, Ying-Cheng Chen, Yong-Fan Chen, and Ite A. Yu. Generation of sub-mhz and spectrally-bright biphotons from hot atomic vapors with a phase mismatch-free scheme. *Opt. Express*, 29(3):4632–4644, 2021.
- [42] L. M. Duan, M. D. Lukin, J. I. Cirac, and P. Zoller. Long-distance quantum communication with atomic ensembles and linear optics. *Nature*, 414:413, 2001.
- [43] Daniel Llewellyn, Yunhong Ding, Imad I. Faruque, Stefano Paesani, Davide Bacco, Raffaele Santagati, Yan-Jun Qian, Yan Li, Yun-Feng Xiao, Marcus Huber, Mehul Malik, Gary F. Sinclair, Xiaoqi Zhou, Karsten Rottwitt, Jeremy L. O’Brien, John G. Rarity, Qihuang Gong, Leif K. Oxenlowe, Jianwei Wang, and Mark G. Thompson. Chip-to-chip quantum teleportation and multi-photon entanglement in silicon. *Nature Physics*, 16(2):148–153, 2020.
- [44] Farid Samara, Nicolas Maring, Anthony Martin, Arslan S. Raja, Tobias J. Kippenberg, Hugo Zbinden, and Rob Thew. Entanglement swapping between independent and asynchronous integrated photon-pair sources. *arXiv:2011.08150*, 2020.
- [45] Francesco Garrisi, Federico Andrea Sabattoli, Nicola Bergamasco, Micol Previde Massara, Federico Pirzio, Francesco Morichetti, Andrea Melloni, Marco Liscidini, Matteo Galli, and Daniele Bajoni. Characterization of photon pairs generated by a silicon ring resonator under electrical self-pumping. *arXiv:2011.03273*, 2020.
- [46] Ran Finkelstein, Eilon Poem, Ohad Michel, Ohr Lahad, and Ofer Firstenberg. Fast, noise-free memory for photon synchronization at room temperature. *Science Advances*, 4(1), 2018.
- [47] M. D. Reid and D. F. Walls. Violations of classical inequalities in quantum optics. *Phys. Rev. A*, 34:1260–1276, 1986.
- [48] P. Grangier, G. Roger, and A. Aspect. Experimental evidence for a photon anticorrelation effect on a beam splitter: A new light on single-photon interferences. *EPL (Europhysics Letters)*, 1(4):173, 1986.
- [49] H. H. Jen. Positive- p phase-space-method simulation of super-radiant emission from a cascade atomic ensemble. *Phys. Rev. A*, 85:013835, 2012.
- [50] C. K. Hong, Z. Y. Ou, and L. Mandel. Measurement of subpicosecond time intervals between two photons by interference. *Phys. Rev. Lett.*, 59:2044–2046, 1987.
- [51] Shengwang Du. Quantum-state purity of heralded single photons produced from frequency-anticorrelated biphotons. *Phys. Rev. A*, 92:043836, 2015.
- [52] Peter J. Mosley, Jeff S. Lundeen, Brian J. Smith, Piotr Wasylczyk, Alfred B. U’Ren, Christine Silberhorn, and Ian A. Walmsley. Heralded generation of ultrafast single photons in pure quantum states. *Phys. Rev. Lett.*, 100:133601, 2008.
- [53] Shengwang Du, Jianming Wen, and Morton H. Rubin. Narrowband biphoton generation near atomic resonance. *J. Opt. Soc. Am. B*, 25(12):C98–C108, 2008.
- [54] A. Mari and J. Eisert. Positive wigner functions render classical simulation of quantum computation efficient. *Phys. Rev. Lett.*, 109:230503, 2012.
- [55] Ivo Straka, Ana Predojević, Tobias Huber, Lukáš Lachman, Lorenz Butschek, Martina Miková, Michal Mičuda, Glenn S. Solomon, Gregor Weihs, Miroslav Ježek, and Radim Filip. Quantum non-gaussian depth of single-photon states. *Phys. Rev. Lett.*, 113:223603, 2014.
- [56] Mikołaj Lasota, Radim Filip, and Vladyslav C. Usenko. Sufficiency of quantum non-gaussianity for discrete-variable quantum key distribution over noisy channels. *Phys. Rev. A*, 96:012301, 2017.

Supplementary material

S1. NUMERICAL MODEL

The starting point of our modeling is Eq. (1) in the main text, provided by Du *et al.* [53], which delineates the bi-photon wavefunction

$$\psi(\tau) = \frac{L}{2\pi} \int d\omega_s \kappa(\omega_s) \text{sinc}\left(\frac{\Delta k L}{2}\right) e^{i(k_s+k_i)L/2} e^{-i\omega_s \tau}. \quad (\text{S1})$$

Here $\kappa(\omega_s)$ is defined as

$$\kappa(\omega_s) = -i \frac{2\sqrt{\bar{\omega}_s \bar{\omega}_i}}{c} \chi^{(3)}(\omega_s) E_p E_c, \quad (\text{S2})$$

where $\bar{\omega}_s$ and $\bar{\omega}_i$ are the central frequencies of the signal and idler photons, $2E_p$ and $2E_c$ are the pump and control electric-field amplitudes, and $\chi^{(3)}(\omega_s)$ is the third-order susceptibility of the atomic medium, which is calculated in Sec. S2 below.

The solid curve $g_{s-i}^{(2)}(\tau)$ in Fig. 3(a) is calculated by convolving $|\psi(\tau)|^2$ with the measured detectors' time jitter. The dashed and solid curves in Fig. 5(b) are the FWHM of $|\psi(\tau)|^2$ before and after the convolution, respectively. The generation rate R is calculated by $R = \int |\psi(\tau)|^2 d\tau$. The single detection count rates in the signal and idler modes are given by $N_s = 2\rho_{22}\Gamma \cdot \text{OD}$ and $N_i = 2\rho_{44}\gamma \cdot \text{OD}$, respectively, where ρ_{jj} is the population in state $|j\rangle$ as denoted in Fig. S1, and 2Γ (2γ) is the decay rate from state $|2\rangle$ ($|4\rangle$). The peak of the normalized cross-correlation and the heralding efficiency are calculated as $[g_{s-i}^{(2)}]_{\text{max}} = |\psi(\tau)|_{\text{max}}^2 / [N_i N_s]$ and $\eta = R/N_i$. No fit parameters are used except for a fixed rescaling factors of $g_{s-i}^{(2)}$, R , and η , common to all data in the paper. All experimental parameters of the system were independently determined from spectroscopic measurements.

S2. SUSCEPTIBILITY CALCULATION

We model our system as an ensemble of four-level atoms shown in Fig. S1. The Hamiltonian in the rotating-wave approximation, assuming a parametric process where $\Delta_s = \Delta_p + \Delta_c - \Delta_i$, is

$$H = \hbar \left[-\Delta_p |2\rangle\langle 2| - \Delta_s |3\rangle\langle 3| - (\Delta_p + \Delta_c) |4\rangle\langle 4| - \left(\Omega_p |2\rangle\langle 1| + \Omega_p^* |1\rangle\langle 2| + \Omega_c |4\rangle\langle 2| + \Omega_c^* |2\rangle\langle 4| + \Omega_i |4\rangle\langle 3| + \Omega_i^* |3\rangle\langle 4| + \Omega_s |3\rangle\langle 1| + \Omega_s^* |1\rangle\langle 3| \right) \right]. \quad (\text{S3})$$

Here Δ and Ω are the fields' detunings and Rabi frequencies, and the subscripts p, c, i, and s stand for pump, control, idler, and signal fields, respectively.

For brevity, we define $\delta = \Delta_p + \Delta_c$ and the following complex decay rates for atoms with velocity v along the optical

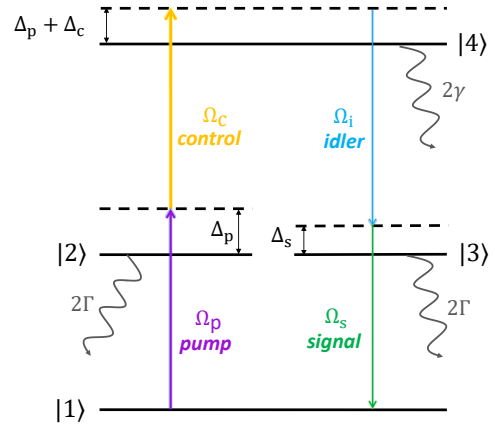


Figure S1. Schematic level structure and optical fields used for calculating the susceptibility.

axis

$$\Gamma_{21}(v) = \Gamma - i(\Delta_p - k_p v) \quad (\text{S4a})$$

$$\Gamma_{31}(v) = \Gamma - i(\Delta_s - k_s v) \quad (\text{S4b})$$

$$\Gamma_{42}(v) = (\Gamma + \gamma) - i(\Delta_c + k_c v) \quad (\text{S4c})$$

$$\Gamma_{43}(v) = (\Gamma + \gamma) + i(\Delta_i + k_i v) \quad (\text{S4d})$$

$$\Gamma_{41}(v) = \gamma - i[\delta - (k_p - k_c)v] \quad (\text{S4e})$$

$$\Gamma_{32}(v) = 2\Gamma - i[\Delta_c - \Delta_i + (k_c - k_i)v]. \quad (\text{S4f})$$

The Master equation for atoms with velocity v gives at the steady-state

$$\dot{\rho}_{21} = 0 = -\Gamma_{21}(v)\rho_{21} + i\Omega_p(\rho_{11} - \rho_{22}) - i\Omega_s\rho_{23} + i\Omega_c^*\rho_{41} \quad (\text{S5a})$$

$$\dot{\rho}_{31} = 0 = -\Gamma_{31}(v)\rho_{31} + i\Omega_s(\rho_{11} - \rho_{33}) - i\Omega_p\rho_{32} + i\Omega_i^*\rho_{41} \quad (\text{S5b})$$

$$\dot{\rho}_{42} = 0 = -\Gamma_{42}(v)\rho_{42} + i\Omega_c(\rho_{22} - \rho_{44}) - i\Omega_p^*\rho_{41} + i\Omega_i\rho_{32} \quad (\text{S5c})$$

$$\dot{\rho}_{43} = 0 = -\Gamma_{43}(v)\rho_{43} + i\Omega_i(\rho_{33} - \rho_{44}) - i\Omega_s^*\rho_{41} + i\Omega_c\rho_{23} \quad (\text{S5d})$$

$$\dot{\rho}_{41} = 0 = -\Gamma_{41}(v)\rho_{41} - i\Omega_p\rho_{42} - i\Omega_s\rho_{43} + i\Omega_c\rho_{21} + i\Omega_i\rho_{31} \quad (\text{S5e})$$

$$\dot{\rho}_{32} = 0 = -\Gamma_{32}(v)\rho_{32} - i\Omega_p^*\rho_{31} - i\Omega_c\rho_{34} + i\Omega_i^*\rho_{42} + i\Omega_s\rho_{12} \quad (\text{S5f})$$

$$\dot{\rho}_{11} = 0 = 2\Gamma\rho_{22} + 2\Gamma\rho_{33} + i\Omega_p^*\rho_{21} - i\Omega_p\rho_{12} + i\Omega_s^*\rho_{31} - i\Omega_s\rho_{13} \quad (\text{S5g})$$

$$\dot{\rho}_{22} = 0 = -2\Gamma\rho_{22} + \gamma\rho_{44} + i\Omega_p\rho_{12} - i\Omega_p^*\rho_{21} + i\Omega_c^*\rho_{42} - i\Omega_c\rho_{24} \quad (\text{S5h})$$

$$\dot{\rho}_{33} = 0 = -2\Gamma\rho_{33} + \gamma\rho_{44} + i\Omega_s\rho_{13} - i\Omega_s^*\rho_{31} + i\Omega_i^*\rho_{43} - i\Omega_i\rho_{34} \quad (\text{S5i})$$

$$\dot{\rho}_{44} = 0 = -2\gamma\rho_{44} + i\Omega_c\rho_{24} - i\Omega_c^*\rho_{42} + i\Omega_i\rho_{34} - i\Omega_i^*\rho_{43}, \quad (\text{S5j})$$

where it is implicit that $\rho_{ij} \equiv \rho_{ij}(v)$.

The third-order susceptibility that generates the signal photons is given by the third-order term in the fields generating the coherence ρ_{31} . Re-arranging Eq. (S5b), we find

$$\rho_{31} = \frac{1}{\Gamma_{31}(v)} \left[i\Omega_s(\rho_{11} - \rho_{33}) - i\Omega_p\rho_{32} + i\Omega_i^*\rho_{41} \right]. \quad (\text{S6})$$

The first term in the brackets on the right-hand side corresponds to the first-order susceptibility, and the second and third terms correspond to the third-order susceptibility.

The relation $|\Omega_p\rho_{32}| \ll |\Omega_i^*\rho_{41}|$ is valid in our experiment for the vast majority of atomic velocities. It is so, as the majority of the population remains in the ground state, and due to the nearly Doppler-free configuration of the $5S_{1/2} \rightarrow 5P_{3/2} \rightarrow 5D_{5/2}$ transitions. We have numerically verified this relation for a wide range of parameters. Therefore, we neglect the second term in the brackets of the right-hand side of Eq. (S6), integrate over all velocities, and arrive at the third-order susceptibility

$$\chi^{(3)}(\Delta_s) = in \frac{\mu_s \mu_i}{\epsilon_0 \hbar E_p E_c} \int dv f(v) \frac{i\Omega_i^*}{\Gamma_{31}(v)} \rho_{41}(v). \quad (\text{S7})$$

Here n is the atomic density, and μ_{13} and μ_{34} are the dipole moments of the $|1\rangle \rightarrow |3\rangle$ and $|3\rangle \rightarrow |4\rangle$ transitions, respectively. $f(v) = \exp(-v^2/(2v_T^2))/(\sqrt{2\pi}v_T)$ is the one-dimensional Maxwell-Boltzmann distribution, and $v_T = \sqrt{k_B T/m}$ is the thermal velocity, where T is the temperature and m is the atomic mass of ^{85}Rb .

We calculate the spinwave coherence per atomic velocity $\rho_{41}(v)$ by neglecting the signal and idler vacuum fields. Therefore, Eq. (S5) is reduced to the Master equation of a three-level ladder system, and we solve it numerically for each v . Doing so, we also get the excited-state populations, used to model the fluorescence into the signal and idler modes.

From Eq. (S6), we find the signal photon's linear susceptibility

$$\chi_s^{(1)}(\Delta_s) = n \frac{|\mu_{13}|^2}{\epsilon_0 \hbar} \int dv f(v) \frac{i(\rho_{11}(v) - \rho_{33}(v))}{\Gamma_{21}(v)}. \quad (\text{S8})$$

The idler photon's linear susceptibility is small and can be neglected.

A note on the weak-pump limit

For completeness, we also solve the steady-state of the Master equation analytically under the weak-pump approximation. To first order in Ω_p and Ω_s , the population remains in the ground state: $\rho_{11} = 1$, $\rho_{22} = \rho_{33} = \rho_{44} = 0$. Under this assumption, Eqs. (S5) for the coherences simplify into two decoupled sets:

$$0 = -\Gamma_{42}(v)\rho_{42} + i\Omega_i\rho_{32}, \quad (\text{S9a})$$

$$0 = -\Gamma_{43}(v)\rho_{43} + i\Omega_c\rho_{23}, \quad (\text{S9b})$$

$$0 = -\Gamma_{32}(v)\rho_{32} - i\Omega_c\rho_{34} + i\Omega_i^*\rho_{42}, \quad (\text{S9c})$$

and

$$0 = -\Gamma_{21}(v)\rho_{21} + i\Omega_p + i\Omega_c^*\rho_{41}, \quad (\text{S10a})$$

$$0 = -\Gamma_{31}(v)\rho_{31} + i\Omega_s + i\Omega_i^*\rho_{41}, \quad (\text{S10b})$$

$$0 = -\Gamma_{41}(v)\rho_{41} + i\Omega_c\rho_{21} + i\Omega_i\rho_{31}. \quad (\text{S10c})$$

We need to solve only the second set. Neglecting terms second-order in Ω_s, Ω_i , we get

$$\rho_{41}(v) = -\frac{\Omega_p\Omega_c}{\Gamma_{21}(v)\Gamma_{41}(v) + |\Omega_c|^2}, \quad (\text{S11})$$

and, using Eq. (S11) in Eq. (S10b), we find

$$\rho_{31}(v) = \frac{i\Omega_s}{\Gamma_{31}(v)} - i \frac{\Omega_c\Omega_p\Omega_i^*}{\Gamma_{31}(v)[\Gamma_{21}(v)\Gamma_{41}(v) + |\Omega_c|^2]}. \quad (\text{S12})$$

The first term corresponds to the linear susceptibility of the signal photon and the second term corresponds to the third-order susceptibility. Hence, the third-order susceptibility averaged over all velocities in the weak-pump limit is

$$\chi^{(3)}(\Delta_s) = \frac{n}{i\epsilon_0\hbar^3} \int dv f(v) \frac{\mu_{31}^*\mu_{43}^*\mu_{21}\mu_{42}}{\Gamma_{31}(v)[\Gamma_{21}(v)\Gamma_{41}(v) + |\Omega_c|^2]}. \quad (\text{S13})$$

S3. COMPARISON OF SINGLE-PHOTON SOURCES

Table S1 shows the data of the heralded single-photon sources used to generate Fig. 1 of the main text. In cases where $[g_{s-i}^{(2)}]_{\max}$ could not be evaluated from the available data, but the coincidence-to-accidentals ratio (CAR) was given, we estimate $[g_{s-i}^{(2)}]_{\max} = 2 \times \text{CAR}$.

Table S1. **Photon source parameters used for compiling Fig. 1 in the main text.** SPDC: Spontaneous parametric down-conversion; FWM: Four-wave mixing; MRR: Microring resonators.

Reference	source	generation rate [kcps]	max cross-correlation
This work	Hot vapor	55*	254*
[41]	Hot vapor	1	42
[8]	Cavity SPDC	6	200**
[41]	Hot vapor	1	42
[9]	Cavity SPDC	0.11	11
[10]	Cavity SPDC	2.5	11.25
[7]	Cavity SPDC	6.1	92**
[5]	Cavity SPDC	0.045	60
[36]	Hot vapor	30	84
[45]	FWM in MRR	26	360**
[39]	Hot vapor	12	360
[33]	Hot vapor	30	126
[35]	Hot vapor	40	6
[40]	Hot vapor	8	97
[29]	Cold atoms	0.031	5800
[4]	Cavity SPDC	8	65
[6]	Cavity SPDC	2.9	40
[44]	FWM in MRR	20	600**
[43]	FWM in MRR	20	100**
[28]	Cold atoms	0.36	20
[11]	Cavity SPDC	2.5	50
[12]	Cavity SPDC	42.5	600**

* One representative point from the curve shown in Fig. 1 of the main text.

** Here, $[g_{s-i}^{(2)}]_{\max}$ is estimated from the coincidence-to-accidentals ratio (CAR).